SUPPORTING INFORMATION

Water splitting for hydrogen chemisorption in graphene oxide dynamically evolving to a graphane character lattice

Laura Ciammaruchi[a,1,*], Luca Bellucci[b*], Gabriel Comerón Castillo[c], Guillermo Martínez-Denegri Sánchez[a], Quan Liu[a], Valentina Tozzini[b], and Jordi Martorell[a,c]

[a]ICFO - Institut de Ciencies Fotoniques, The Barcelona Institute of Science and Technology, Castelldefels 08860, Spain

[b]NEST - Istituto Nanoscienze del CNR and Scuola Normale Superiore, P.zza S. Silvestro 12, Pisa 56127, Italy

[c]Departament de Física, Universitat Politècnica de Catalunya, Terrassa 08222, Spain

[1]Present Address: ICMAB - Institut de Ciència de Materials de Barcelona, Campus de la UAB - Bellaterra 08193, Spain

[*]Corresponding authors. E-mail: lciammaruchi@icmab.es (Laura Ciammaruchi); luca.bellucci@nano.cnr.it (Luca Bellucci)

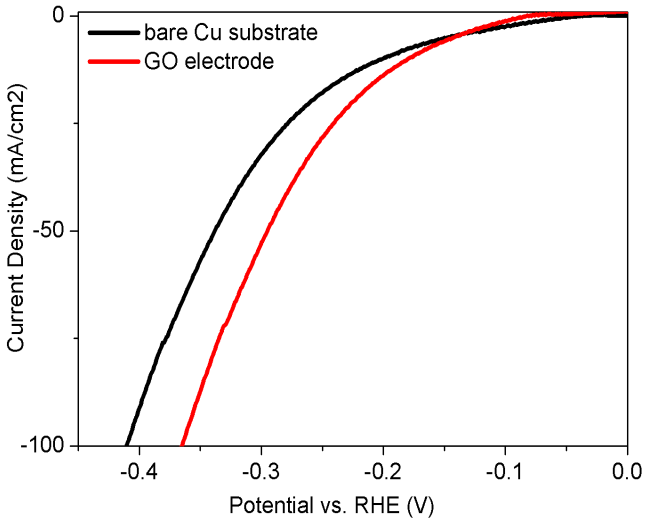

Figure S1 - HER polarization curves for Cu and GO-based electrodes working in alkaline solution

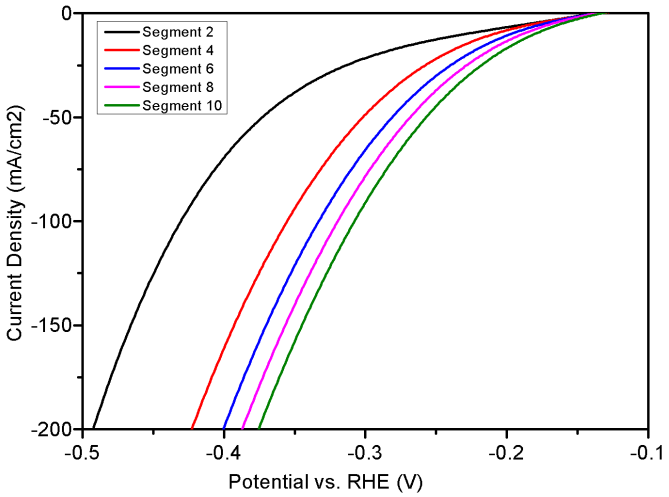

Figure S2 - HER Polarization curves (0.01V/s, 0.01M KOH) of GO-based electrode at subsequent sweeping intervals, 40 minutes apart (segment 2: 40min; segment 4: 80min; segment 6: 120 min; segment 8: 160 min; segment 10: 200min).

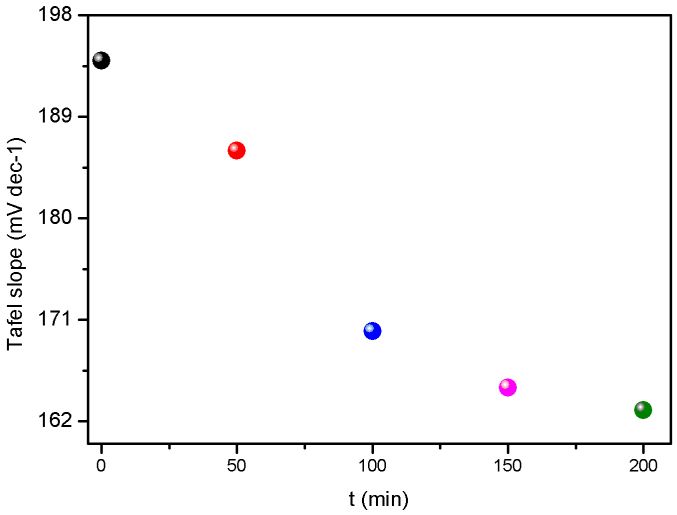

Figure S3 - Tafel slopes of GO-based electrode as a function of sweeping time

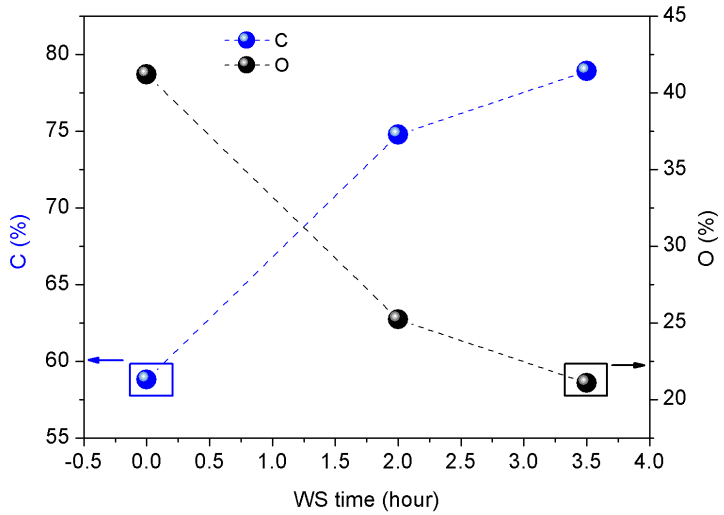

Figure S4 - EDX quantitative elemental data of Carbon and Oxygen presence (at.%) in the GO material as a function of WS time

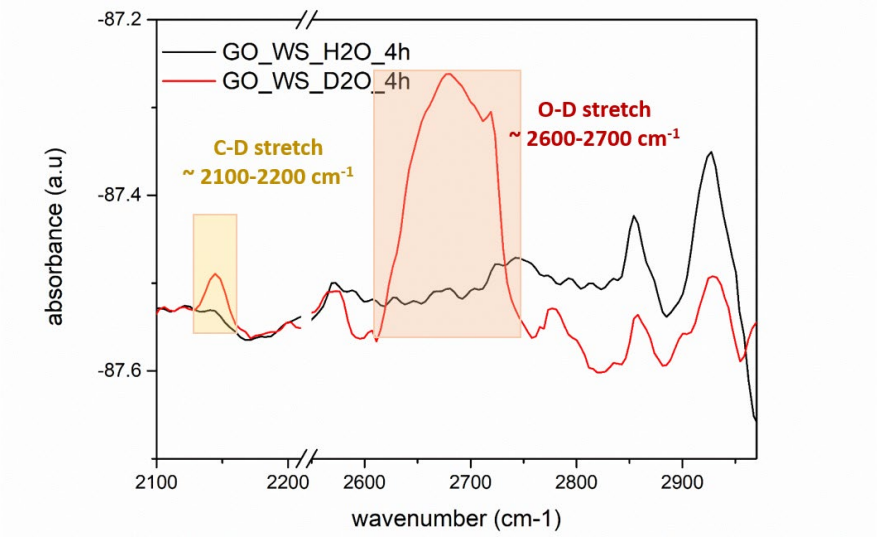

Figure S5 - FTIR spectra of GO electrodes after 4h –long WS in regular (black) and deuterated (red) water. In the latter, two new peaks arise at ~ 2100cm^{-1} and ~ 2600cm^{-1}, corresponding to the C-D and O-D stretching modes. A spectrum break in the (2300-2500) cm^{-1} range is applied for clarity. Power spectra obtained from MD simulation of the hydrogenated/deuterated systems clearly show the fingerprint bands at ~ 2900 cm^{-1}, typical of the presence of stable C-H bonds, and C-D bonds at ~ 2100 cm^{-1}.

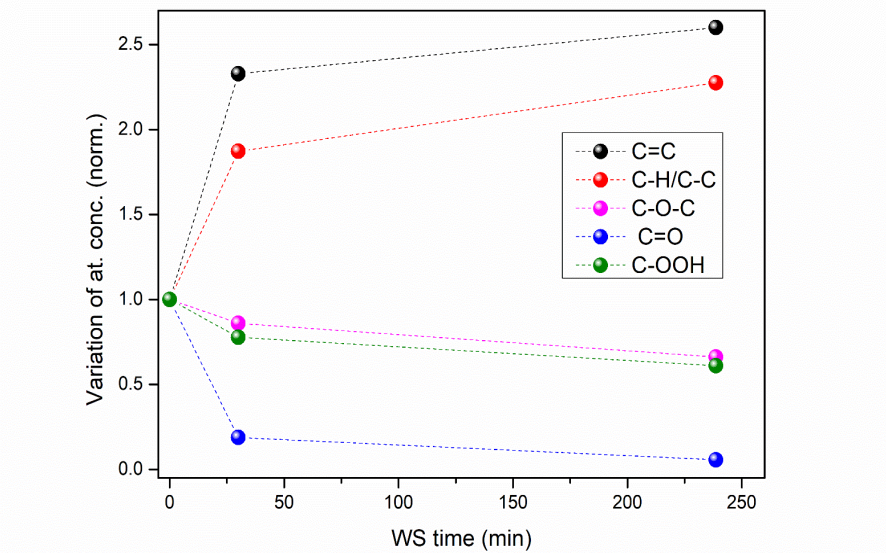

Figure S6 - Normalized variation of Carbon functionalities at different WS times, from C1s XPS data

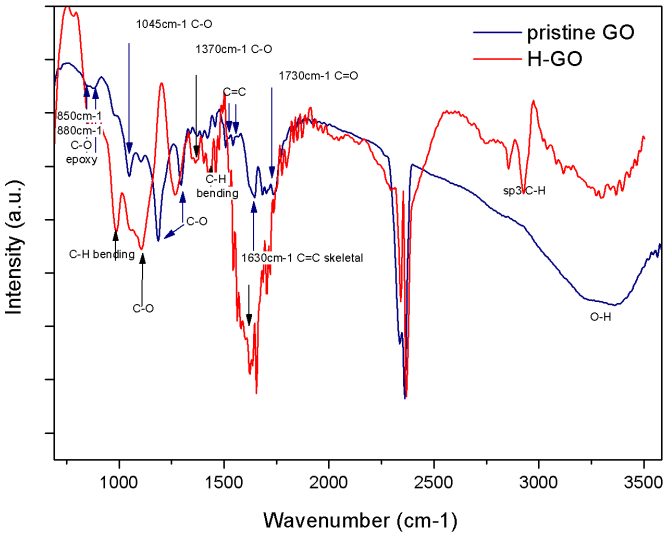

Figure S7 - FTIR spectroscopy of pristine GO material (blue) and reduced/hydrogenated GO after 4-h WS (red). Pristine GO was deposited on top of a Zinc Sulfide substrate and measured in transmission mode, while H-GO was deposited on a Cu electrode and measured in reflection mode.

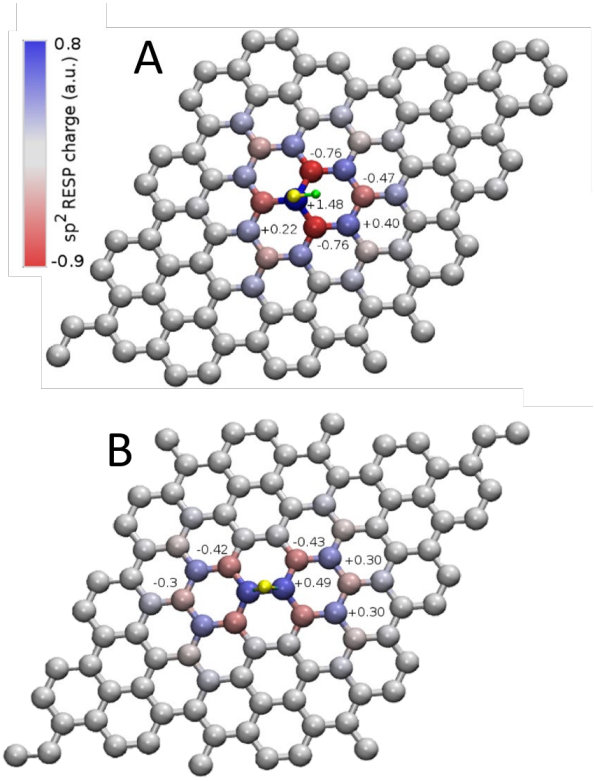

Figure S8 - (a) Polarization map induced by a hydroxyl group. The positive partial charge localized on the sp3 atoms induces a negative partial charge in its first sp2 neighbors, and a positive charge - reduced in intensity - in the second neighbors, and so on. (b) Polarization map induced by an epoxy group. In this configuration, the absolute RESP charge values are overall less intense than in configuration (a).

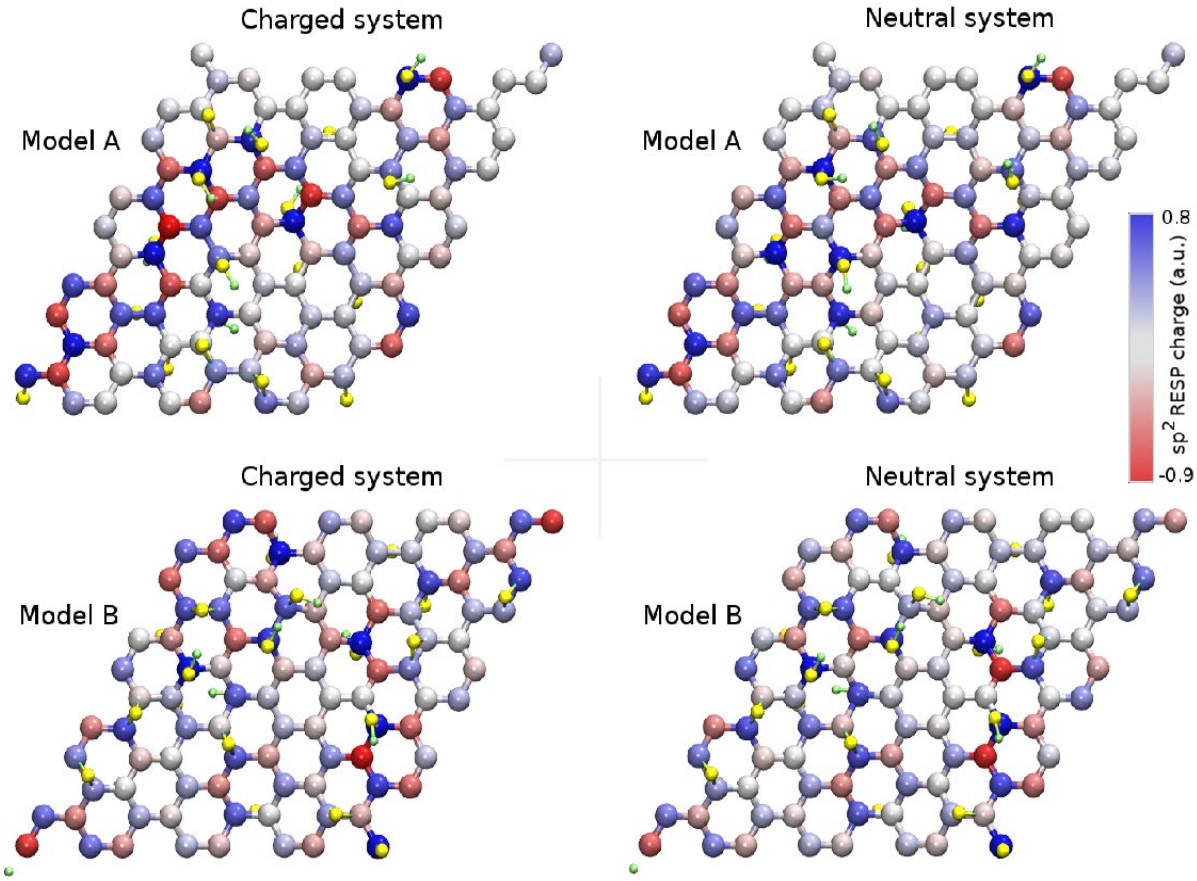

Figure S9 - Comparison between distributions of the RESP derived partial charges for charged (rGO^{-2}) and neutral (rGO) systems. Left: maps of the charged systems MA and MB. Right: maps of the neutral systems.

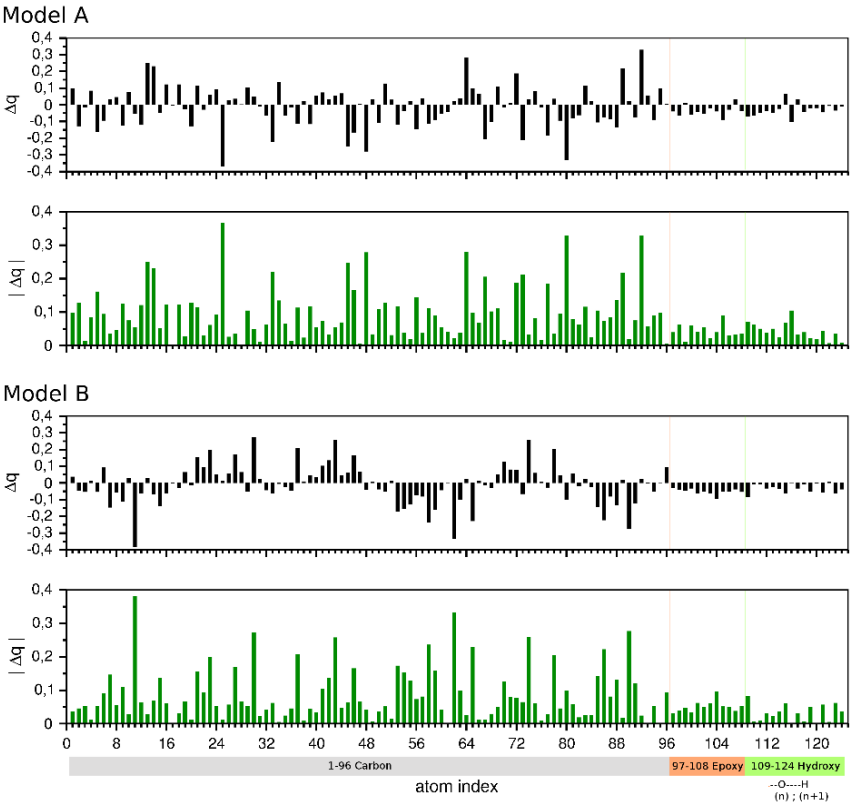

Figure S10 - $\Delta q = q_{rGO-2} - q_{rGO}$ and its absolute value $|\Delta q|$ with respect the atoms, for systems MA (top) and MB (bottom).

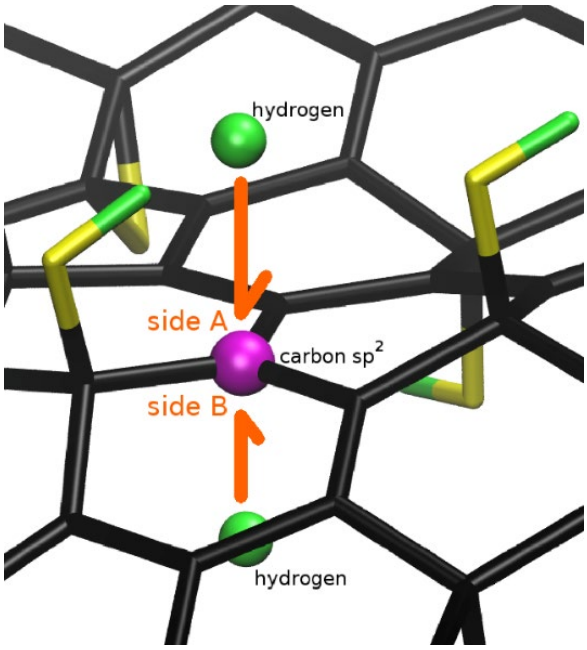

Figure S11 - Proton placement in front of the sp2 carbon lattice, simulating the Volmer step of HER

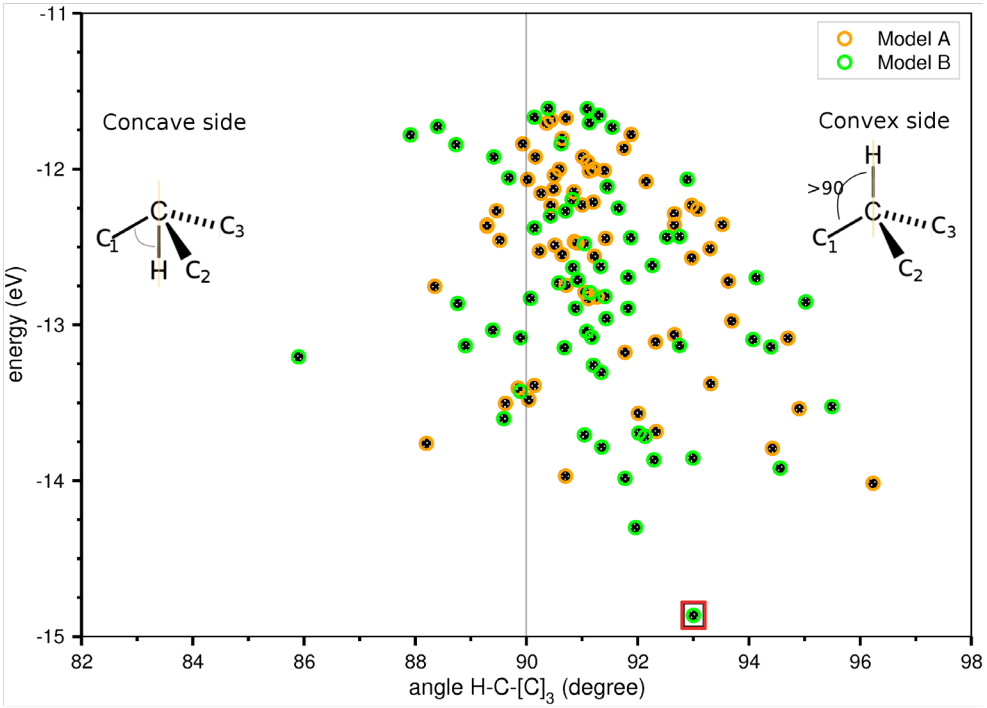

Figure S12 - Minimum energy values of the total chemisorption energy for both models MA/MB as a function of the initial average angle defined between the H-C bond and the 3 carbon neighbours of the hydrogenated C atom, (i.e. H-C-$[C]_3$). The angle is evaluated before the minimization and it defines the concave/convex H position with respect the carbon atom. H is placed 1 Å away from the central C atom along the perpendicular axis of the plane defined by the 3 C atoms (C_1 C_2 and C_3) and passing through the central C atom. If the average angle values is greater than 90 degree, H is on the convex side (right side of the figure), otherwise is on the concave side of the lattice (left side of the figure). After minimization, H placed on the convex side get energetically favoured conformations. Value in the red square has the lowest energy value and it corresponds to the structure of Fig. S17.b

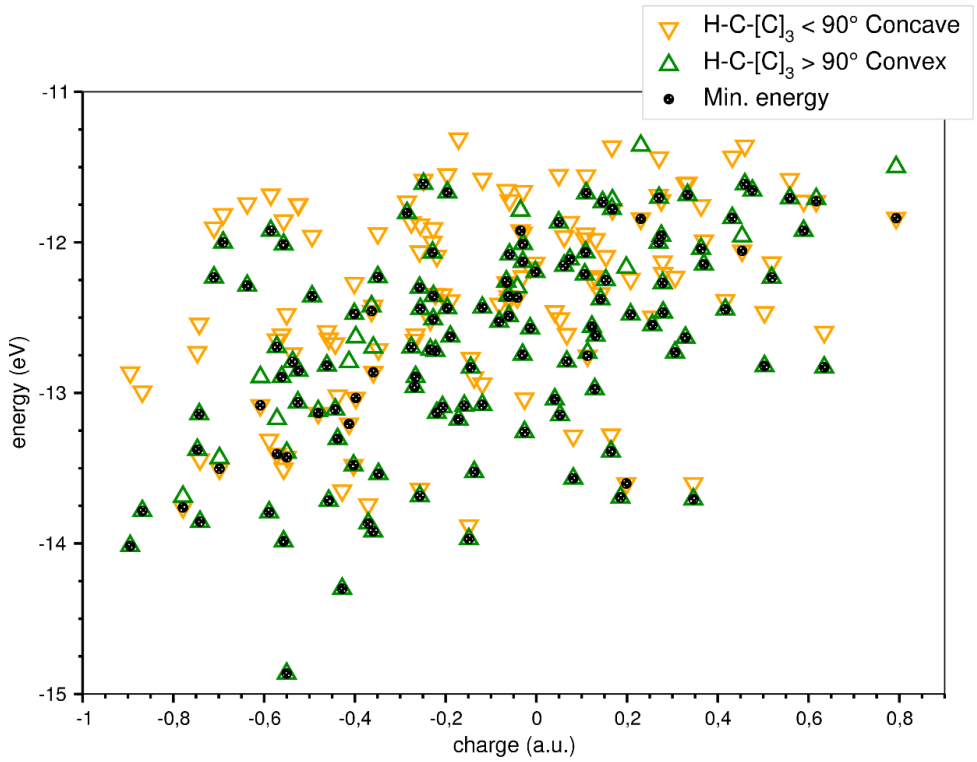

Figure S13 - All energy values of the total chemisorption energy for both models MA/MB as a function of partial charges. The hydrogens preferentially attach on the locally convex sites of the lattice (green triangles). Both models display a soft correlation between the total chemisorption energy and the RESP derived carbon charge values.

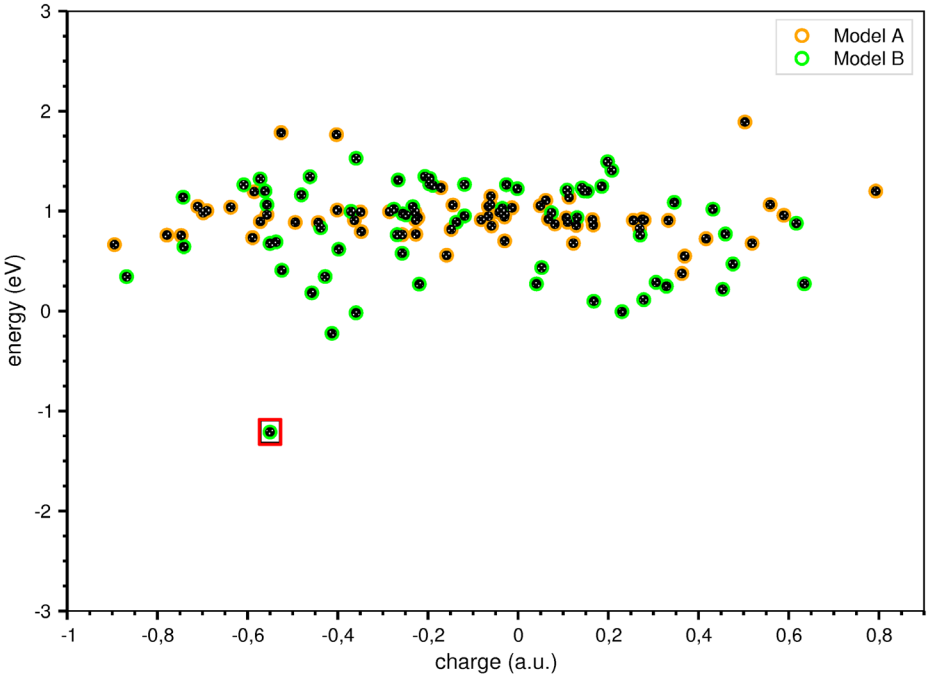

Figure S14 - Conformational energy ΔE^{conf} as a function of carbon partial charges. Red square highlights the lowest and most favorable conformational energy due to a severe rearrangement of the lattice (Fig S17).

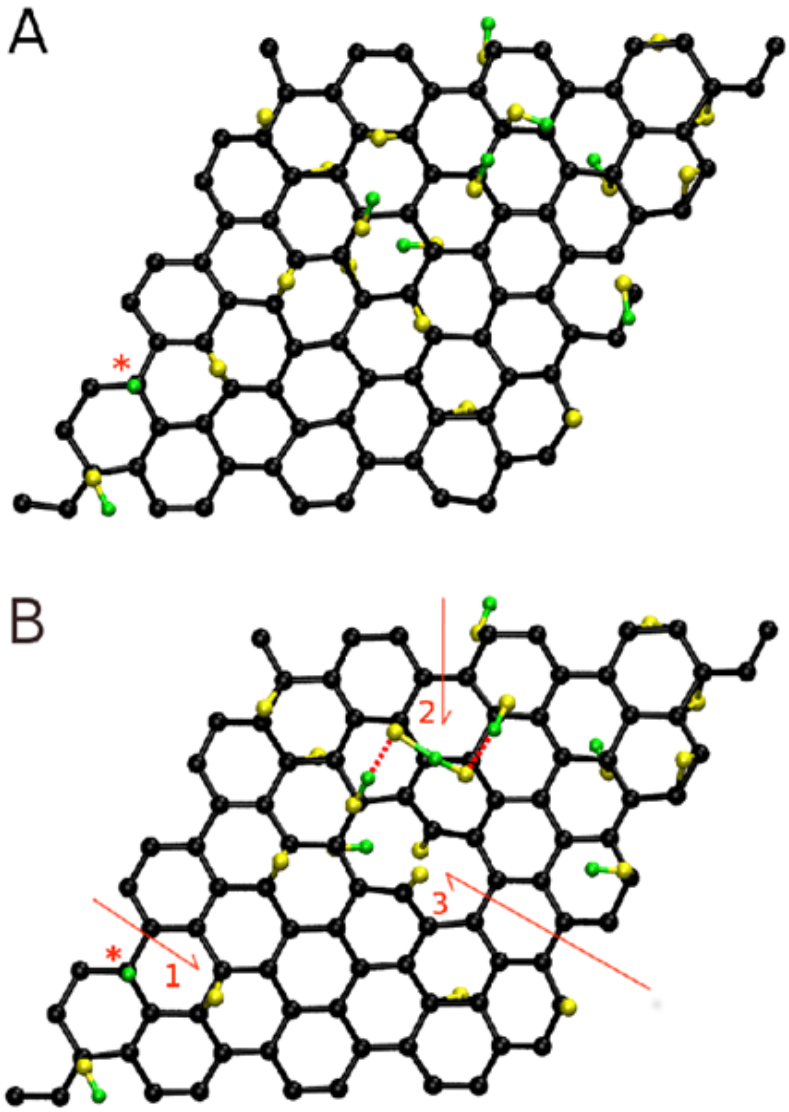

Figure S15 - Structure at the beginning (A) and after minimization (B) of the protonated system at its lowest energy. The red asterisk labels the C-H at the initial (A) and final (B) position. Numbered arrows highlight the most important structural changes of the minimized lattice with respect to the initial structure: (1) the change of the epoxide group, (2) the formation of peculiar network of hydrogen bond and (3) the opening of two ring with formation of ketones.

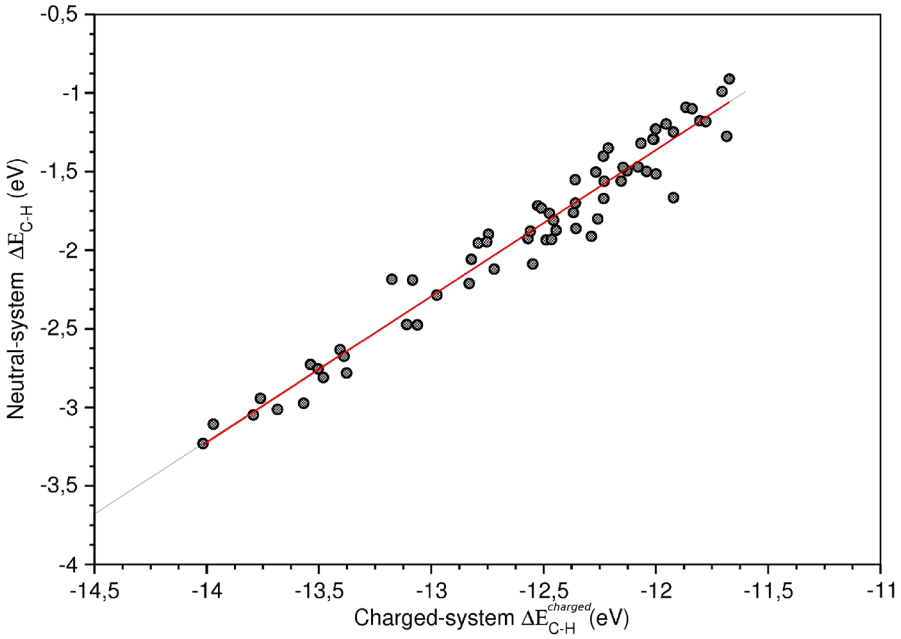

Figure S16 - $\Delta E^{neutral,C-H}$ vs $\Delta E_{C\text{-}H,\ charged}$. The relationship between C-H bond stabilization energies in the neutral and charged system is linear: $\Delta E^{neutral,C-H} = 9.8 + 0.93\ \Delta E_{C\text{-}H,\ charged}$

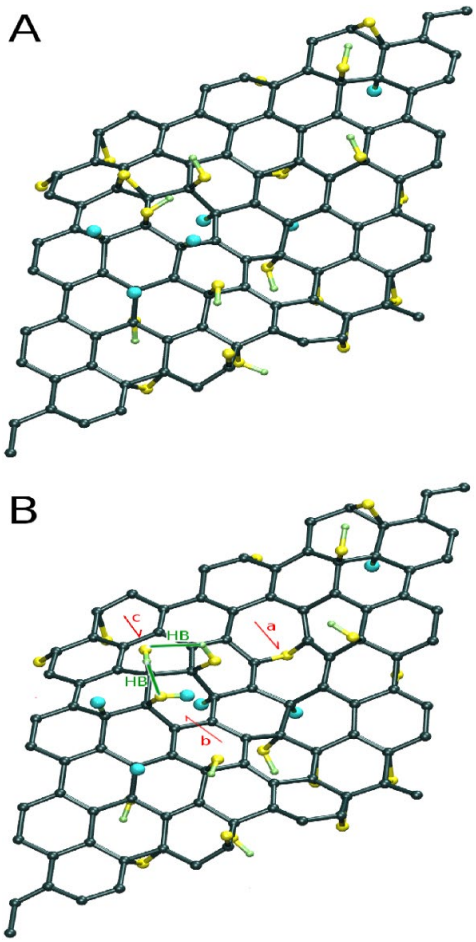

Figure S17 – HrGO before (A) and after (B) a 10-ps MD simulation at 300 K (see Methods). The HrGO model was derived by placing the most stable hydrogen atom in the sp^2 carbon atoms proximity. Hydrogens attached to the carbon atom are in light blue. During the MD simulation, the lattice undergoes certain conformational rearrangements, pointed out by the red arrows in (B): the opening of an epoxy ring (^{a}), the splitting of C-H (^{b}), and the formation of a new -OH group (^{c}). The conformational rearrangement occurred between a C-H and its neighbour hydroxyl group is such that H detaches from the carbon and attaches to the hydroxyl group, which in turns transfers its hydrogen

to the adjacent epoxy group, to finally form a stable partner of hydroxyl groups sharing a peculiar network of hydrogen bonds. In green the Hydrogen Bond (HB) network arising from the C-H splitting and the formation of the new –OH.

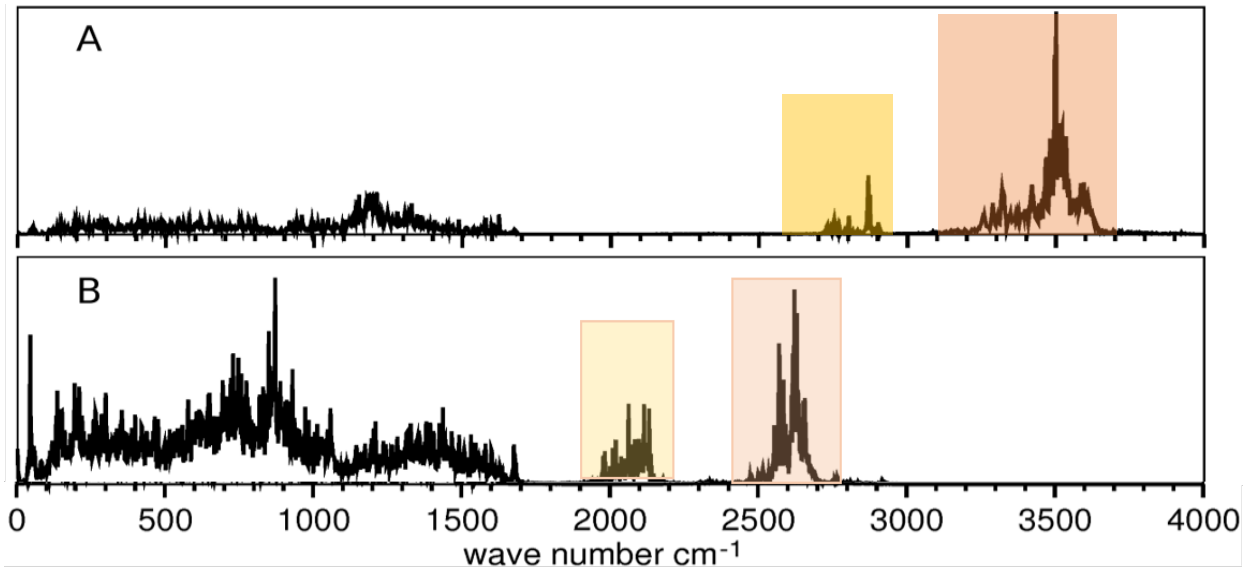

Figure S18 - (A) Power spectra (PS) of the hydrogenated system (H_6rGO); the typical sp3 C-H peak fingerprint shows up at around 2900 cm^{-1} and OH groups at 3500 cm^{-1} (B) SP for the hydrogenated system, where all hydrogen atoms are substituted with deuterium (D-rGO). The C-D peak is shifted at lower wavelengths, at around 2100 cm^{-1}, and the hydroxyl groups become deuterated. The O-D modes appear at around 2600 cm^{-1}.

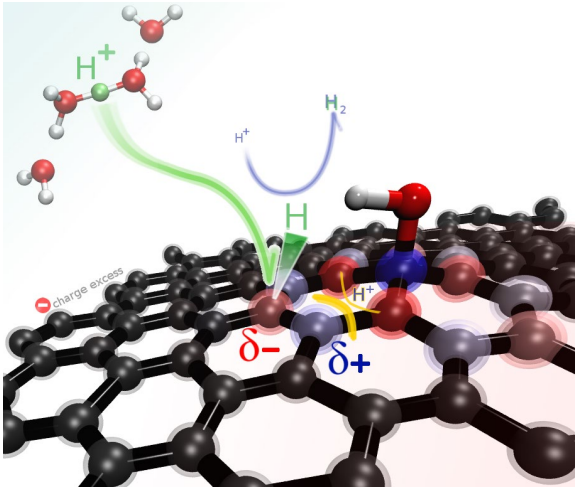

Figure S19 - Outline of the C-H bond formation process on GO. At first, H^+ (green) is mainly driven by the electrostatic interaction with the electrode's negative charge excess. Even though H^+ preferentially attaches on the convex side of the most negatively charged carbon (red carbon atom), the final C-H stabilization is largely influenced by the chemisorption-induced structure relaxation, together with further conformational rearrangement. While hydrogen will be released in the form of H_2 gas for the most part, stable C-H may form after the potential release. Indeed, the H_2 release *via* the Heyrovsky reaction (blue arrows) is unlikely due to the low proton concentration (pH> 10), whereas the release *via* Tafel reaction is hindered due to the adsorption instability induced by the positive partial charge of the polarized carbon (highlighted in yellow).

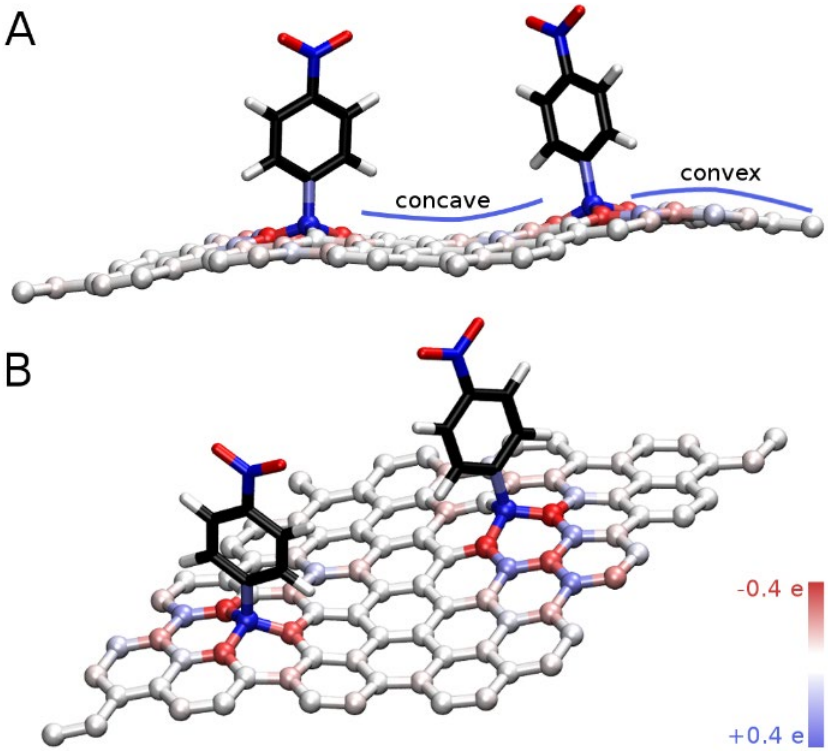

Figure S20 – H-chemisorption may be modulated by tailoring graphene-based materials with functional groups, like for example nitrobenezene. (A) Nitrobenzene composites attached to the rGO lattice are shown to functionalize the rGO lattice by creating convex and concave areas able to shape the lattice geometry. (B) Local polarization effect of the lattice due to nitrobenzene functionalization.

Table S1 - Carbon and Oxygen at. conc. % extrapolated from EDX elemental composition analysis for the pristine GO and GO after 4-hour long WS experiment.

XPS values	C 1s (at %)	O 1s (at %)
GO_PRISTINE	51.968	48.033
GO_4h WS	77.076	22.924

Note S1

The hydrogen evolution reaction (HER) polarization curve for a GO electrode working in alkaline solution is depicted in (Fig. S1), where the increased GO activity over the bare Cu substrate is evident. As a comparison, the HER curve on bare Cu electrode is included. The GO time-dependent HER enhancement suggests that the GO material behaves as a H* adsorption acceptor in the Volmer-Heyrovsky-Tafel route for HER[1,2] (Fig. S2). Indeed, the hydrogen adsorption step on the electrode surface (i.e. Volmer step: $H+ e^- \rightarrow H^*$) is usually followed by either chemical (i.e Tafel step: $H^* + H^* \rightarrow H_2$) or electrochemical (i.e Heyrovsky step: $H^+ + H^* + e^- \rightarrow H_2$) hydrogen desorption[3,4]. Working in alkaline environment can make the HER exchange currents slow down, making the Volmer stage the rate-determining step of the overall reaction[5,6]. This assumption seems confirmed by the Tafel slope values extrapolated from time-dependent HER curves (Fig. S3), ranging from ~ 200 mV/dec (first scan) to 160 mV/dec (last scan, 200min). These values are in good agreement with published results[7] and may well indicate that the initial proton adsorption is the rate-determining step of the whole HER process.

Note S2

The Raman spectrum deconvolution of pristine GO shows the three main Raman features[8–10]: a D band located at ~ 1350 cm^{-1}, a G band positioned at ~ 1588 cm^{-1}, and D' peak at ~ 1609 cm^{-1}. The G peak is the result of in-plane vibrations of sp^2 bonded carbon atoms, and it corresponds to the E_{2g} phonon at the Brillouin zone center (Γ point), while the D and D' bands are defect-activated peaks corresponding to single phonon intervalley and intravalley scattering events, respectively[11]. The D band is due to out-of-plane vibrations attributed to the presence of structural defects (breathing modes), but is not sensitive to the defect geometry, the D' band instead has a dependency on the nature of lattice defect[8]. D, G and D' bands were identified and deconvoluted by applying the Second Derivative Method routine present in the Origin Pro 8 package, in which hidden peaks are revealed by detecting local minima in the raw Raman spectrum. As for the change in spectral features, the D band height increase is commonly related to the presence of a higher number of broken sp^2 carbon rings, while its broadening should correspond to the presence of smaller sp^2 clusters and chains embedded in an increasingly defective matrix. Such sp^2 rings disruption is known to be related to the presence of grain boundaries, vacancies, as well as to sp^3-hybridized C-C bonds.

The relatively high number of graphene layers produces a broad 2D peak at around 2700 cm^{-1} [12].

Upon reduction, it has been reported[13–15] that the 2D peak red-shifts together with and intensity increase, whilst its FWHM shrinks. Indeed, when comparing the 2D Raman spectra of pristine GO vs. material that underwent a 4h-long water splitting process (see figure below), we find out that: the 2D peak position shifts from ~ 2700cm^{-1} to ~ 2683cm^{-1}, the relative FWHM shifts from ~ 285 cm^{-1} to ~ 221 cm^{-1} and the 2D intensity (units normalized to G peak) goes from 0.069 to 0.095.

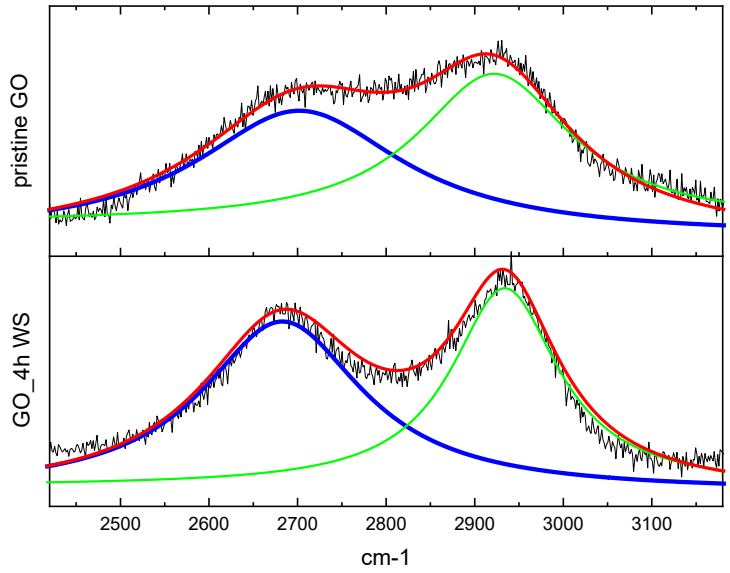

In the table below we report the exact peaks values after deconvolution:

2D	Peak position (cm^{-1})	FWHM (cm^{-1})	Intensity (norm. u.)
Pristine GO	2701,92	284,23	0,0697
GO_4h WS	2682,83	221,3	0,095

Abundant literature discusses the best way to fit Raman spectra of graphene-based materials[16,17]. Generally speaking, the final observed spectral distribution can be interpreted as a convolution of intrinsic+extrinsic contributions. In broad terms, the extrinsic contribution can be considered coming from the measurement apparatus, and is conventionally represented as having a Gaussian shape. Intrinsic (excitation/de-excitation) processes giving rise to the actual signal instead, can be described by an exponential decay having a finite lifetime, therefore corresponding to a Lorentzian line shape.

The total line shape is then a convolution of Gaussian and Lorentzian, also called "Voigt" profile. The "peudo-Voigt" profile - frequently used for calculations of experimental spectral line shapes - is an approximation of the Voigt profile that uses a linear combination of a Gaussian and Lorentzian, instead of their convolution.

Note S2

As the WS experiment and the graphene hydrogenation take place, we register an evolution of all the main Raman features over time. For each peak, position and FWHM were averaged over at least 6 similar measurements.

Table S2.1 – Averaged positions and FWHM values of D, G, and D' peaks, for pristine and hydrogenated material.

	D		**G**		**D'**	
	Pristine	**4h_WS**	**Pristine**	**4h_WS**	**Pristine**	**4h_WS**
<Position> ± St Dev (cm^{-1})	1352,3 ± 0,39	1347,11± 0,89	1588,72 ± 3,19	1574,26 ± 2,68	1608,59 ± 0,46	1599,87 ± 0,56
<FWHM> ± St Dev (cm^{-1})	87,29 ± 1,17	152,67 ± 2,29	88,19 ± 0,86	108,59± 0,81	51,09 ± 1,05	66,33 ± 1,36

Note S3

WS control experiments were realized in virtually identical working conditions as those described in the Methods, except for the use of deuterated water in exchange for regular deionized water. The resultant FTIR spectrum for the deuterated material shows C-D[18] and O-D[19] modes at their typical vibration frequencies (Fig. S5). This cross-check let us rule out the presence of any potential interference in the final result shown in Fig. 2a, as due to specific experimental procedure followed.

Note S4

The starting complex electrode-electrolyte interface[20,21] was conveniently streamlined with a model consisting of an GO sheet in vacuum with a fixed charge excess of 2e-, able to mimic the cathode charge excess induced by the applied potential. The charge excess per atom is 0.016e- (2e-/124 atoms) and it is of the same magnitude as the average carbon atoms charge of a graphene-based electrode with an applied potential of 2V[22]. A value of 0.01 e^- per atom was also used[23] to model a set of grephene-based electrodes with fixed charge, and it corresponded to the average charge of carbon atoms having an applied potential of 1V. Since the number of final chemisorbed hydrogens is related to the amount of available carbons prone to chemisorb H, the final amount of C-H bonds formed will be proportional to the material's specific surface area and abundance.

Note S5

The stability of a chemisorbed proton onto rGO was evaluated by comparing its energy with respect to the unprotonated rGO system. The neutral mono-hydrogenated system (H-rGO) - as well the mono-negatively charged system (rGO^-) count an odd number of electrons. The treatment of such systems requires the use of spin-polarized calculation with alpha and beta orbitals, which in turn doubles the computational cost. To reduce such cost, rGO is preliminary modelled by adding two negative charges to the neutral system (rGO^{-2}). An even number of electrons in the system eliminates

the use of explicit spin orbitals, and at the same time does mimick the actual charge excess at the cathode.

As well, the mono-hydrogenated system H-rGO^{-1} is modelled by adding a proton to rGO^{-2}, and is then followed by minimization. The Volmer reaction step can then be schematized as follows:

$$rGO^{-2}+H^{+}\rightarrow HrGO^{-}$$

Note S6.1

The relative $HrGO^{-}$ stability with respect to rGO^{-2} can be estimated as the difference between the energy of the whole system E_{HrGO-}, and the sum of the two isolated systems E_{H+} and E_{rGO-2}. In first approximation, the energy of the non-interacting proton (E_{H+}) can be considered as an additive constant and is numerically evaluated to be =-1 eV**.** In other terms:

$$\Delta E_{C-H,\ charged}=E_{HrGO}{}^{-}-(E_{H}{}^{+}+E_{rGO}{}^{-2})$$

Note S6.2

With an approach similar to Note F.1, starting from the optimized structure HrGO^{-1}, we can also obtain the neutral system HrGO by depriving HrGO^{-1} of an electron, and then minimizing it by means of spin polarized orbitals. The total HrGO system energy (E_{HrGO}) and the energy of the neutral system (E_{rGO}) and the atomic hydrogen (E_H) were used to evaluate energy of the C-H in a neutral configuration:

$$\Delta E_{C-H}=E_{HrGO}-(E_H+E_{rGO})$$

Where E_H was numerically evaluated by calculating the total energy of the atomic hydrogen in vacuum, and amounted to E_H=-13.48 eV**.** Such computational protocol has been similarly reported to evaluate the adsorption/chemisorption energy of chemical species on graphene[24–28].

During the first HER step, the proton chemisorbing on rGO is mainly driven by the electrostatic interaction due the excess electrons of the cathode. This chemisorption is finally modulated by the local atomic features of the lattice, as the proton "prefers" to attach onto the convex side of negatively charged carbon atoms (Fig. S13).

After the potential release, the excess charge disappears from the electrode and the proton may remain chemisorbed onto the carbon in a C-H bond. In this configuration, the proton charge and the electrode charge excess neutralize each other and as a result, the electrostatic contribution is no more present. At this point he C-H stability mainly relies on the "chemical" contribution, i.e. on the stability of the C-H covalent bond (i.e. ΔE_{C-H}). Indeed, after the potential release the excess charge disappears from the electrode but the proton may remain chemisorbed onto the carbon in a C-H bond. The C-H covalent bond energy (ΔE_{C-H}) is evaluated by subtracting the energy of the neutral and isolated species (E_H and E_{rGO}) from the energy of the hydrogenated GO (E_{HrGO}).

Note S7

In order to evaluate the conformational energy ΔE^{conf} we estimated it as the energy of the "frozen" $HrGO^{-}$system conformation, deprived of the H^{+} atom ($E_{*rGO}{}^{-2}$). The conformational term was then written as:

$$\Delta E^{conf.}=E_{*rGO}{}^{-2}-E_{rGO}{}^{-2}.$$

References

1 D. M. F. Santos, C. a. C. Sequeira and R. F. M. Lobo, *Int. J. Hydrogen Energy*, 2010, **35**, 9901–9909.

2 C. A. C. Sequeira, D. M. F. Santos, J. R. Sousa and P. S. D. Brito, *Mater. Technol.*, , DOI:10.1179/175355509X460659.

3 A. R. Kucernak and C. Zalitis, *J. Phys. Chem. C*, 2016, **120**, 10721–10745.

4 D. M. F. Santos, C. A. C. Sequeira and J. L. Figueiredo, *Quim. Nova*, 2013, **36**, 1176–1193.

5 W. Sheng, H. A. Gasteiger and Y. Shao-Horn, *J. Electrochem. Soc.*, 2010, **157**, B1529.

6 K. Zeng and D. Zhang, *Prog. Energy Combust. Sci.*, 2010, 36, 307–326.

7 Y. Zheng, Y. Jiao, L. H. Li, T. Xing, Y. Chen, M. Jaroniec and S. Z. Qiao, *ACS Nano*, 2014, **8**, 5290–5296.

8 S. Ghosh, K. Ganesan, S. R. Polaki, T. R. Ravindran, N. G. Krishna, M. Kamruddin and A. K. Tyagi, *J. Raman Spectrosc.*, 2014, **45**, 642–649.

9 L. M. Malard, M. A. Pimenta, G. Dresselhaus and M. S. Dresselhaus, *Phys. Rep.*, 2009, 473, 51–87.

10 A. C. Ferrari, *Solid State Commun.*, 2007, **143**, 47–57.

11 A. C. Ferrari and D. M. Basko, *Nat Nano*, 2013, **8**, 235–246.

12 A. A. K. King, B. R. Davies, N. Noorbehesht, P. Newman, T. L. Church, A. T. Harris, J. M. Razal and A. I. Minett, *Sci. Rep.*, 2016, **6**, 19491.

13 Y. Hao, Y. Wang, L. Wang, Z. Ni, Z. Wang, R. Wang, C. K. Koo, Z. Shen and J. T. L. Thong, *Small*, , DOI:10.1002/smll.200901173.

14 Z. Luo, T. Yu, K. J. Kim, Z. Ni, Y. You, S. Lim, Z. Shen, S. Wang and J. Lin, *ACS Nano*, 2009, **3**, 1781–1788.

15 Y. Shen and A. C. Lua, *Sci. Rep.*, , DOI:10.1038/srep03037.

16 A. C. Ferrari and J. Robertson, *Philos. Trans. R. Soc. A Math. Phys. Eng. Sci.*, 2004.

17 F. C. Tai, S. C. Lee, J. Chen, C. Wei and S. H. Chang, *J. Raman Spectrosc.*, , DOI:10.1002/jrs.2234.

18 J. K. Chin, R. Jimenez and F. E. Romesberg, *J. Am. Chem. Soc.*, 2001, 123, 2426–2427.

19 T. Schäfer, J. Lindner, P. Vöhringer and D. Schwarzer, *J. Chem. Phys.*, , DOI:10.1063/1.3151673.

20 A. Roldan, *Curr. Opin. Electrochem.*, , DOI:10.1016/j.coelec.2018.03.013.

21 E. Skúlason, V. Tripkovic, M. E. Björketun, S. Gudmundsdóttir, G. Karlberg, J. Rossmeisl, T. Bligaard, H. Jónsson and J. K. Nørskov, *J. Phys. Chem. C*, 2010, **114**, 18182–18197.

22 C. Xu, B. Xu, Y. Gu, Z. Xiong, J. Sun and X. S. Zhao, *Energy Environ. Sci.*, 2013, **6**, 1388.

23 C. Merlet, C. Péan, B. Rotenberg, P. A. Madden, P. Simon and M. Salanne, *J. Phys. Chem. Lett.*, 2013, **4**, 264–268.

24 D. Chanda, J. Hnát, A. S. Dobrota, I. A. Pašti, M. Paidar and K. Bouzek, *Phys. Chem. Chem. Phys.*, 2015, **17**, 26864–26874.

25 A. S. Dobrota, I. A. Pašti, S. V. Mentus and N. V. Skorodumova, *Phys. Chem. Chem. Phys.*, 2016, **18**, 6580–6586.

26 A. S. Dobrota, I. A. Pašti, S. V. Mentus and N. V. Skorodumova, *Phys. Chem. Chem. Phys.*, 2017, **19**, 8530–8540.

27 Y. Jiao, Y. Zheng, K. Davey and S.-Z. Qiao, *Nat. Energy*, 2016, **1**, 16130.

28 S. Zhou and A. Bongiorno, *Acc. Chem. Res.*, 2014, **47**, 3331–3339.